JACS
JOURNAL OF THE AMERICAN CHEMICAL SOCIETY
Article
pubs.acs.org/JACS

Symmetry-Supported Magnetic Blocking at 20 K in Pentagonal Bipyramidal Dy(III) Single-Ion Magnets

Yan-Cong Chen,[†] Jun-Liang Liu,[*,†] Liviu Ungur,[*,‡,§] Jiang Liu,[†] Quan-Wen Li,[†] Long-Fei Wang,[†] Zhao-Ping Ni,[†] Liviu F. Chibotaru,[‡] Xiao-Ming Chen,[†] and Ming-Liang Tong[*,†]

[†]Key Laboratory of Bioinorganic and Synthetic Chemistry of Ministry of Education, School of Chemistry and Chemical Engineering, Sun Yat-Sen University, Guangzhou 510275, P. R. China

[‡]Theory of Nanomaterials Group and INPAC—Institute of Nanoscale Physics and Chemistry, Katholieke, Universiteit Leuven, 3001 Leuven, Belgium

[§]Theoretical Chemistry, Lund University, 22241 Lund, Sweden

Supporting Information

ABSTRACT: Single-molecule magnets (SMMs) that can be trapped in one of the bistable magnetic states separated by an energy barrier are among the most promising candidates for high-density information storage, quantum processing, and spintronics. To date, a considerable series of achievements have been made. However, the presence of fast quantum tunnelling of magnetization (QTM) in most SMMs, especially in single-ion magnets (SIMs), provides a rapid relaxation route and often sets up a limit for the relaxation time. Here, we pursue the pentagonal bipyramidal symmetry to suppress the QTM and present pentagonal bipyramidal Dy(III) SIMs $[Dy(Cy_3PO)_2(H_2O)_5]Cl_3\cdot(Cy_3PO)\cdot H_2O\cdot EtOH$ (**1**) and $[Dy(Cy_3PO)_2(H_2O)_5]Br_3\cdot 2(Cy_3PO)\cdot 2H_2O\cdot 2EtOH$ (**2**), (Cy_3PO = tricyclohexyl phosphine oxide). Magnetic characterizations reveal their fascinating SMM properties with high energy barriers as 472(7) K for **1** and 543(2) K for **2**, along with a record magnetic hysteresis temperature up to 20 K for **2**. These results, combined with the *ab initio* calculations, offer an illuminating insight into the vast possibility and potential of what the symmetry rules can achieve in molecular magnetism.

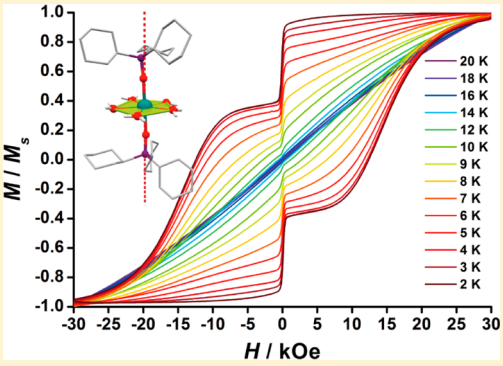

INTRODUCTION

Single-molecule magnets (SMMs) have attracted unprecedented interest in recent years across many fields, including chemistry, physics, and material science.[1−6] The early age of single-molecule magnets mainly focused on the polymetallic clusters of transition metal ions toward the combination of large spin states and high anisotropies.[7] However, it was extremely difficult for chemists to achieve both criteria because the increase of total spins by adding metal ions usually resulted in more symmetrical molecular structures that frequently counteracted the anisotropies. Later, the introduction of lanthanide ions into SMMs brought new light to this field, owing to the intrinsic large spin state and large magnetic anisotropy of some lanthanide ions, especially Tb(III), Dy(III), Ho(III), and Er(III).[8−12] The recent focus on organometallic SMMs went a step further, as the usual coordination environments and structures can be stabilized, thus permitting huge anisotropies.[13] Specifically, the radical-bridged dilanthanide complexes have provided some of the best candidates, with record blocking temperatures up to 14 K.[14−16]

On the other hand, as an interesting subgroup, the monometallic SMMs or single-ion magnets (SIMs) do not share the commensurable achievements.[9,12,17−22] The major problem encountered here is the fast quantum tunnelling of magnetization (QTM) of the single ion without exchange couplings to suppress it, which limits the relaxation time. Because the QTM comes from the overlap of wave functions which suggests the magnetization no longer conserves over time, the crystal-field theory provides a highly useful guide for some specific, local symmetries to minimize the QTM.[23] A large number of excellent SIMs can be categorized into these local symmetries, especially D_{4d} for square antiprismatic[9,21,22,24] and $D_{\infty h}$ for linear 2-coordinated[17−19] and sandwich-type complexes.[12,25,26]

From the crystal field viewpoint, the pentagonal bipyramidal D_{5h} is also a promising symmetry for SIMs, but it has not been well studied.[27] Although the perfect 5-fold symmetry is forbidden in conventional crystals with translational symmetry, the approximation for the local symmetry around metal ions is achievable by rational design and/or assembly.[28,29] To continue understanding such a strategy and to explore the ultimate limit and potential of SIMs, herein we report the fascinating magnetic blocking behavior in the self-assembled pentagonal

Received: December 31, 2015
Published: January 31, 2016

DOI: 10.1021/jacs.5b13584
J. Am. Chem. Soc. 2016, 138, 2829−2837

bipyramidal complexes $[Dy(Cy_3PO)_2(H_2O)_5]Cl_3\cdot(Cy_3PO)\cdot H_2O\cdot EtOH$ (**1**) and $[Dy(Cy_3PO)_2(H_2O)_5]Br_3\cdot 2(Cy_3PO)\cdot 2H_2O\cdot 2EtOH$ (**2**), (Cy_3PO = tricyclohexylphosphine oxide). Both complexes exhibit high energy barriers, namely, 472(7) K for **1** and 543(2) K for **2**, and their magnetic hysteresis loops remain open up to at least 11 K for **1** and 20 K for **2**, thereby setting a new record.

RESULTS AND DISCUSSION

Crystal Structures. Both complexes are synthesized in a H_2O/EtOH mixed solution via slow evaporation, and the final products are stable in ambient conditions. This characteristic is quite different from most of the organometallic SMMs, which are vulnerable to air and moisture, and such stability provides great convenience for postsynthetic treatment and/or further fabrication in devices. Both complexes can be viewed as self-assembled by Dy(III), Cy_3PO ligands, anions, and solvent molecules; thus, they share a similar $[Dy(Cy_3PO)_2(H_2O)_5]^{3+}$ motif (Figure 1a,b). On the other hand, they still exhibit obvious differences in the outer coordination spheres connected with hydrogen bonds (Figure 1c,d).

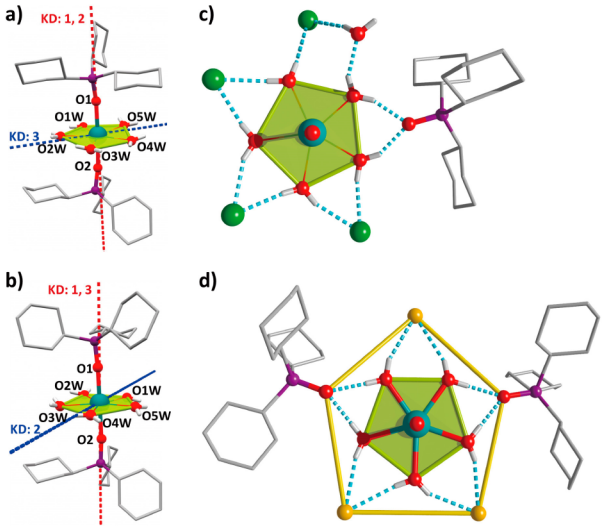

Figure 1. Crystal structures of **1** (a,c) and **2** (b,d). (a,b) Coordination environment of Dy(III) in **1** (a) and **2** (b). (c,d) Outer coordination sphere, connected with hydrogen bonds, in **1** (c) and **2** (d). H atoms of the ligands are omitted for clarity. Color codes: Dy, cyan; P, purple; Br, orange; Cl, green; O, red; C, gray; H, light gray. Red dashed lines passing through O1 and O2 in (a) and (b) represent the main anisotropy axes in the ground KD of these compounds determined by the *ab initio* calculations. The blue dashed lines show the main anisotropy axes in the excited Kramers doublet (KD) through which the activated relaxation proceeds.

Complex **1** crystallizes in the monoclinic space group $P2_1/n$. Each asymmetric unit contains one Dy^{3+} ion, two coordinated ligands in the opposite direction, five coordinated waters in the equatorial plane, one free organic ligand, three Cl^- ions in the outer coordination spheres, and two solvent molecules. The coordination environment for Dy(III) is a compressed pentagonal bipyramid with average Dy−O distances of 2.219 Å (axial) and 2.359 Å (equatorial). Indeed, the polyhedron is quite regular, with an axial O1−Dy−O2 angle of 175.79(14)° and five equatorial O−Dy−O angles ranging from 69.70(16)° to 74.32(15)°. An 11-membered ring is formed by the five coordinated waters and the atoms in the outer coordination spheres, including one Cl^- ion from the neighboring motif (Figure 1c). The intermolecular hydrogen bonds connect the $[Dy(Cy_3PO)_2(H_2O)_5]^{3+}$ motifs side by side and lead to the extended one-dimensional chains packing along the *a* axis (Figure S1), while the interchain interactions are mostly van der Waals forces.

By replacing the anions with Br^-, complex **2** can be obtained and will crystallize in the monoclinic space group *C*2/*c*. Each asymmetric unit contains one Dy^{3+} ion, two coordinated ligands in the opposite direction, five coordinated waters in the equatorial plane, two free organic ligands, three Br^- ions in the outer coordination spheres, and the disordered solvent molecules in the voids between molecules. The pentagonal bipyramidal coordination for Dy(III) in **2** is further compressed, with average Dy−O distances of 2.200 Å (axial) and 2.352 Å (equatorial). A noticeable difference is the shrinkage of the outer coordination spheres to a 10-membered ring, namely, a five-pointed star (Figure 1d). Such a pattern is in favor of the closer approximation to an ideal D_{5h} symmetry, even compared with {Zn_2Dy} with an O−Dy−O angle of 168.6°.[27] Indeed, an O1−Dy−O2 angle of 179.04(11)° and the five equatorial O−Dy−O angles in the range of 70.71(11)−73.24(11)° approach the ideal pentagonal bipyramid, namely, 180° and 72° (Table 1).

Table 1. Selected Bond Lengths (Å) and Bond Angles (deg) for 1 and 2

bond length	1	2
Dy−O1	2.217(4)	2.189(3)
Dy−O2	2.221(4)	2.210(3)
Dy−O1W	2.327(5)	2.365(3)
Dy−O2W	2.355(4)	2.344(3)
Dy−O3W	2.363(4)	2.355(3)
Dy−O4W	2.370(4)	2.362(3)
Dy−O5W	2.382(4)	2.336(3)
bond angle	**1**	**2**
O1−Dy−O2	175.79(14)	179.04(11)
O1W−Dy−O2W	74.32(15)	70.71(11)
O2W−Dy−O3W	71.69(15)	71.44(11)
O3W−Dy−O4W	69.70(16)	71.99(11)
O4W−Dy−O5W	72.24(15)	72.76(11)
O5W−Dy−O1W	72.44(15)	73.24(11)

The Dy(III) ions in both complexes are well separated, with minimum distances of 11.75 Å in **1** and 11.23 Å in **2**, and there are no direct or superexchange routes for magnetic coupling, especially for **2**, where even intermolecular hydrogen bonds are absent (Figure S2). Thus, they are great platforms to study the magnetic relaxations and blockings of individual Ln(III) ions as well-defined SIMs.

Magnetic Characterization. The variable-temperature magnetic susceptibilities are measured on polycrystalline samples of **1** and **2** under a 1 kOe dc field (Figure 2). At room temperature, the χ_mT values for **1** and **2** are, respectively, 13.87 and 13.80 $cm^3\ K\ mol^{-1}$, lower than that expected for a free Dy^{3+} ion (14.17 $cm^3\ K\ mol^{-1}$) due to the splitting of the $^6H_{15/2}$ ground state. Upon cooling, χ_mT in both cases stays essentially constant with only a little decrease, which is evidence of very large magnetic anisotropies with far-separated energy levels, as also indicated by the unsaturated magnetization of approximately 5 Nβ (Figure 3). At the lower temperature end, dynamic magnetic behaviors are observed through the sudden

DOI: 10.1021/jacs.5b13584
J. Am. Chem. Soc. 2016, 138, 2829−2837

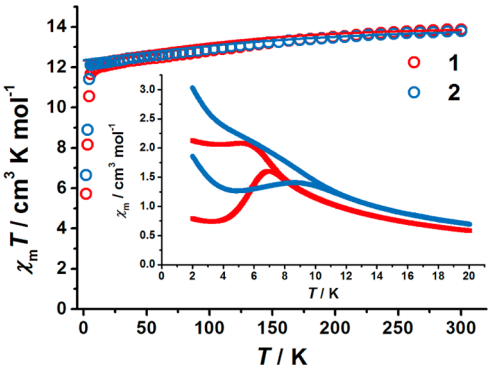

Figure 2. Temperature dependence of the molar magnetic susceptibility $\chi_m T$ products and the zero-field-cooled/field-cooled (ZFC-FC) magnetic susceptibilities. The dc magnetic susceptibilities were collected under a 1 kOe dc field for **1** (red) and **2** (blue). The solid lines correspond to the *ab initio* calculations. The ZFC-FC magnetic susceptibilities (inset) were measured under a 1 kOe dc field in warm mode (2 K/min) and show clear magnetic blocking, with divergences below 8 K for **1** and 11 K for **2**.

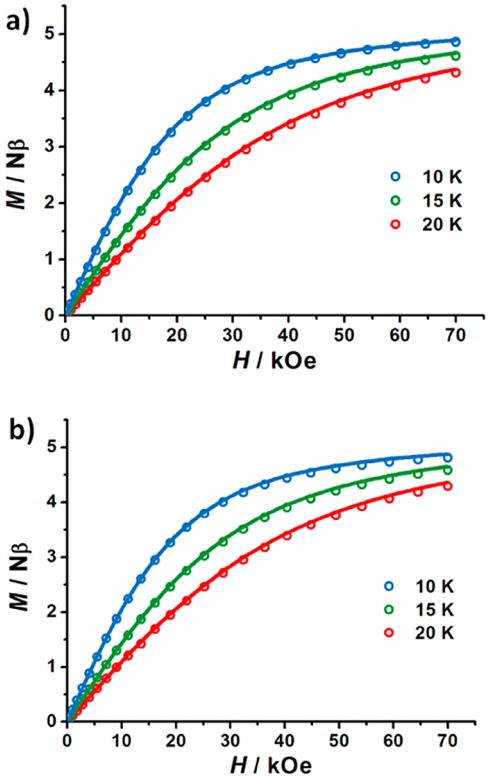

Figure 3. Variable-field magnetization data for **1** (a) and **2** (b). Data were collected from 0 to 7 T in steady fields, while in even lower temperatures slow relaxation of magnetization was observed and resulted in hysteresis. The solid lines correspond to the *ab initio* calculations.

drop of $\chi_m T$ values even in the settle mode with stepped cooling. In the sweeping mode, the zero-field-cooled/field-cooled (ZFC-FC) magnetizations (inset of Figure 2) show clear divergences below 8 K for **1** and 11 K for **2**, corresponding to the process of magnetic blocking.

Variable-temperature and variable-frequency magnetic susceptibilities were also measured in the zero dc field to reveal the dynamic magnetic behaviors of **1** and **2** (Figure 4a,b). The temperature dependence data show typical patterns for SMMs, with the highest peak temperature (1488 Hz) of 28.5 K for **1** and 35 K for **2**. The peaks for different frequencies appear one after another, and the frequency-dependent data (Figure 4c,d) show the clear and steady shift of the peaks toward the low frequency region, without the sign of overwhelming QTM. For most of the reported SMMs, especially SIMs, the QTM usually sets up a limiting relaxation time, and the application of a dc field can significantly affect the ac behavior by suppressing the QTM. However, the application of a 1 kOe dc field on both complexes exhibits little effect on the ac magnetic susceptibilities, which is also evidence that the QTM regime has not yet been encountered.

For the high temperature region, the ac susceptibilities can be fitted with a generalized Debye model (Figure 5a,b), with narrow distributions indicated by the small coefficients α = 0.032−0.087 (16−32 K) for **1** and 0.031−0.16 (16−36 K) for **2**. The relaxation shows significant temperature dependency in great accordance with the Arrhenius law as $\tau = \tau_0 \exp(-U_{eff}/kT)$, corresponding to the Orbach process, and the best fit gives U_{eff} = 472(7) K, $\tau_0 = 8.7 \times 10^{-12}$ s for **1** and U_{eff} = 543(2) K, $\tau_0 = 2.0 \times 10^{-11}$ s for **2** (Figure 6), which are almost unaffected whether a dc field is applied (Figure 5c,d and 6). As a step forward, the dc magnetic relaxation serves as a powerful tool for extending the measuring range and demonstrates the fascinating magnetic behaviors in the lower temperature region. After the removal of a saturated field of 30 kOe, the remnant magnetization shows steady decay upon time, obeying an exponential law (Figure S5). In this extended region, the relaxation time for **1** rises to the order of 10^{-1} s and starts to bend, ending up as 12.1(2) s at 2 K, while for **2** the deviation happens much later, around the order of 10^0 s, and finally reaches 21.3(3) s at 2 K. Here, the effect of the unsuppressed QTM can be observed; thus, the effect of external dc fields starts to appear. When a final 1 kOe dc field is held, a significant increase of the gradients of $\tau - T^{-1}$ curves is observed, resulting in a continuous lengthening of the relaxation times. Compared with the higher temperature region, the temperature-dependent relaxation tends to obey the power law as $\tau \sim T^{-n}$ instead (Figure 6c,d).The best fit gives n = 5.7 for **1** and n = 5.6 for **2**, indicating the involvement of direct/Raman process as commonly observed in the SMMs with extremely long relaxation times. From the measured data range, the relaxation time τ for **1** reaches 1163.2(1) s at 3.5 K, while for **2**, the relaxation rate is too slow; instead, τ = 1409(2) s at 5 K is highlighted (Figure 6c,d).

Because the relaxation has become so slow, clear magnetic hysteresis loops are highly expected and are experimentally observed (Figure 7). Both complexes show typical butterfly-shape hysteresis loops at 2 K, arising from the faster relaxation around the zero field and slower relaxation in the medium fields. Both complexes retain large magnetization, only dropping when H < 200 Oe, which can be attributed to the unsuppressed QTM from the deviation of the symmetry, the hyperfine interaction, and the dipolar interactions. With increasing temperature, the hysteresis loops become narrower as the relaxation speeds up and result in smaller coercive fields and remnant magnetizations (Figure S6). The hysteresis loops remain open up to at least 11 K for **1** and 20 K for **2** (inset of Figure 7), which is unprecedented. This is followed by the record-holding N_2^{3-} radical-bridged $\{Tb_2N_2\}$[15] and $\{Er_2(COT'')_3\}$ (COT″ = 1,4-bis(trimethylsilyl)-cyclooctatetraenyl dianion), which show magnetic hysteresis up to 14 K.[30] It is also worth noting that the coercive fields for

DOI: 10.1021/jacs.5b13584
J. Am. Chem. Soc. 2016, 138, 2829−2837

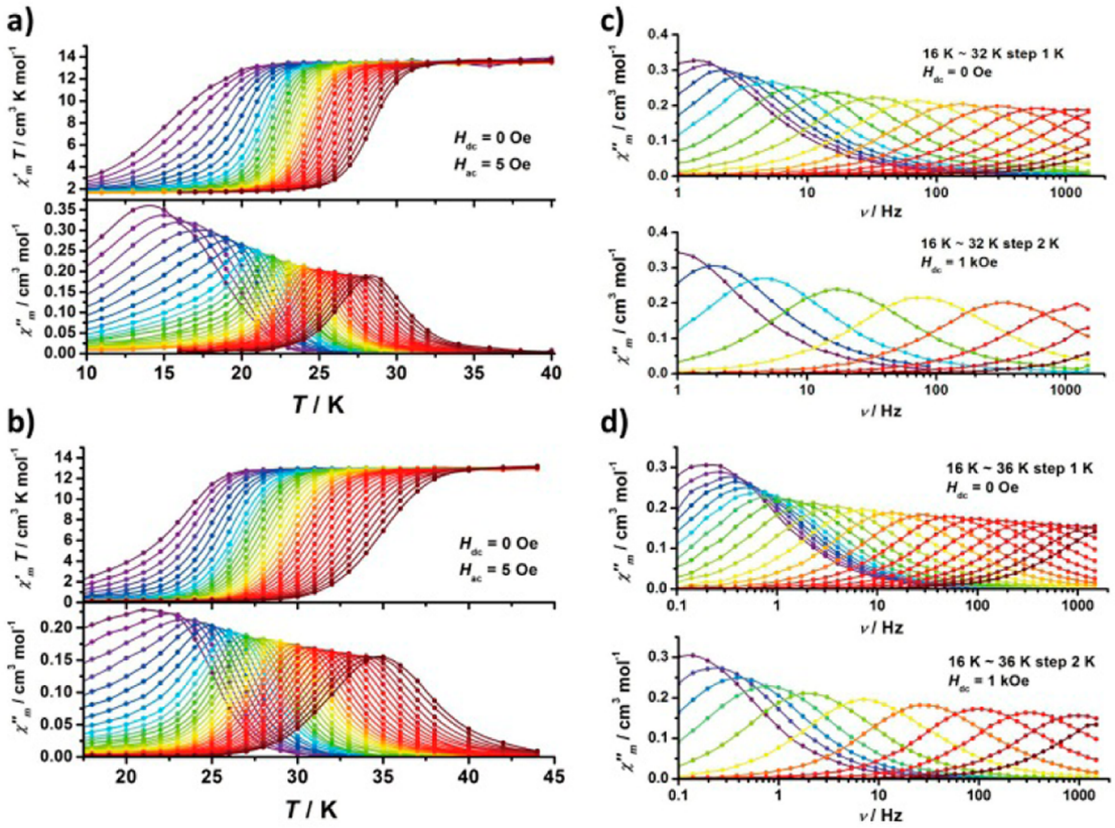

Figure 4. Alternating-current molar magnetic susceptibilities for **1** (a,c) and **2** (b,d). (a,b) Temperature dependence of the in-phase χ'_mT product and out-of-phase χ''_m in a zero dc field for **1** (a) and **2** (b), with ac frequencies of 1−1488 Hz. (c,d) Frequency dependence of the out-of-phase χ''_m in a zero dc field (above) and a 1 kOe dc field (below) for **1** (c) and **2** (d). Lines are to guide the eyes.

2 reach 12.5 kOe at 2 K, among the highest coercive fields for SMMs.

To further elucidate the magnetic blocking, diluted samples **1**@Y and **2**@Y were synthesized with Dy:Y = 1:19 to weaken the dipolar interactions. As expected, the magnetic hysteresis loops for diluted samples only show minor differences near the zero field, indicating the slowing down of the magnetic relaxation to some extent. The hysteresis loops still remain open up to 11 K for **1**@Y and 20 K for **2**@Y, but the opening becomes clearer (Figure 8). Additional ac magnetic susceptibilities were also measured for **1**@Y (Figures S7−S10). With **1**@Y and **1** having similar, long Dy···Dy distances, the results show no significant difference compared with **1** regardless whether in the zero dc field or in the applied dc field (Figure 9), further proving that all of them are well-defined SIMs.

***Ab Initio* Calculations.** Further insight into the electronic structure and magnetic blocking in the investigated dysprosium complexes was obtained through the use of *ab initio* calculations. X-ray geometries of both compounds were employed in the theoretical calculations "as is", without any optimization of the structures by computational means. This factor may undoubtly lower the accuracy of the calculated energy spectrum. Nevertheless it does not affect the basic insight drawing from these calculations concerning the properties of the Kramers doublets (KDs) responsible for the observed relaxation of magnetization in these compounds (vide infra). Table 2 lists the calculated low-lying energy spectrum corresponding to the ground manifold $J = 15/2$ of Dy^{3+} free ion and magnetic anisotropy of individual doublet states.

The main anisotropy axes (g_Z) of the ground states of **1** and **2** are almost collinear to the two shortest chemical bonds of the Dy, O1−Dy−O2 (see Figure 1). Exact deviation angles are given in the SI. The strong axial nature of the ligand field experienced by the Dy site is due to the short and axial nature of these two axial ligands. In particular, we notice that the magnetic axiality ($g_Z/g_{X,Y}$) of the ground state is higher in **2** compared to **1** by almost 1 order of magnitude, which explains the differences of their magnetic behavior in the low-temperature regime, seen in strongly differing magnetic hysteresis loops (Figures 7 and 8). Table 3 shows the parameters of the crystal field obtained from the *ab initio* calculations. The negative sign of B_{20} in both compounds contributes to the stabilization of the wave function of the type $\pm|15/2\rangle$ in the ground state.

In general, the limit of the blocking barrier in lanthanide-based molecular magnets is defined by the DyO^+ ion.[31] All real/model compounds lacking perfect axial symmetry may only approach this generic blocking barrier predicted for this model compound, but never overcome it. In this small biatomic entity, the axial ligand field is purely axial, and the height of the blocking barrier reaches approximately 2200 cm^{-1}/3000 K.[31] This idea was further exploited for several bicoordinated models.[32] In the present case, the five water molecules may be regarded as magnetically innocent in spite of their apparently weak interaction with the Dy site. However, the nonaxial ligand field in these compounds is mostly due to the water molecules, which deviate from the ideal pentagonal arrangement. However, the geometry of pentagonal bipyramid is still one of the best candidates in consideration of (1) the stability of the

DOI: 10.1021/jacs.5b13584
J. Am. Chem. Soc. 2016, 138, 2829−2837

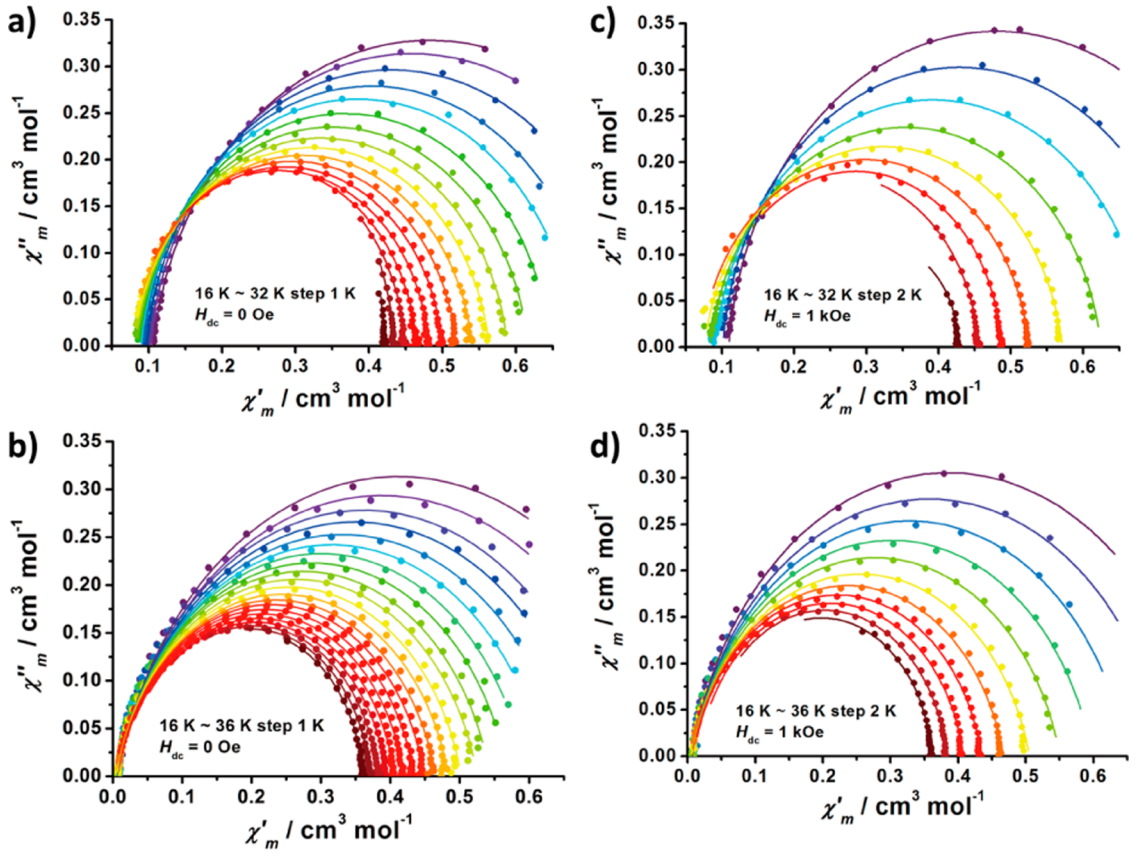

Figure 5. Cole−Cole plots for the ac susceptibilities in a zero dc field for **1** (a) and **2** (b) and in a 1 kOe dc field for **1** (c) and **2** (d) The solid lines are the best fit to Debye's law.

molecules compared to the linear coordinate compounds; (2) minimizing the nonaxial ligand field in this geometry compared to the others, such as trigonal bipyramid, octahedron, and hexagonal bipyramid. Counterions are located farther away from the Dy site and, therefore, do not contribute much to the perpendicular crystal-field exerted on the Dy site.

To understand the origin of the large differences in the magnetization blocking barriers in the investigated compounds, we follow the previously proposed methodology for the investigation of the blocking barrier structure.[33] In this method, the low lying spin−orbit energy states are arranged according to their intrinsic magnetic moment (x axis) and energy (y axis). The average values of the transition magnetic moment between all the states are calculated and displayed. The blocking barrier of the investigated compound is formed by the most probable relaxation route from the state in the maximal magnetization (−1) toward the state with opposite magnetization (+1). Magnetic relaxation will follow the minimum energy path for which transition matrix elements connecting all intermediate states are the largest. Note the relatively small value of the matrix element connecting the components of the ground doublet state in the investigated compounds (Figure 10). This means that the QTM process will be rather weak and suppressed. At high temperatures, when the first excited doublet states are populated (i.e., states 2+ and 2-) a shortcut of the barrier can occur. In **1**, given that the energy of the second excited state (3+ and 3-) is quite close to the energy of the first excited state, while the matrix element between 3+ and 3- is nearly 2 orders of magnitude larger, we may assume that the relaxation rate of the process involving the second excited state is dominant at high temperatures.

In both complexes the blocking barrier becomes shortcut at the lowest excited KD with the main magnetic axis almost perpendicular to the ground one (Figure 1a,b). This is in full accord with the earlier finding that the transverse magnetic matrix element between the components of the two doublets increases dramatically with the angle between their main magnetic axes.[31] Indeed, Figure 10 shows that despite the high axiality of the KDs defining the top of the barriers in **1** and **2**, with g_Z approaching the values in the ground KD (last column in Table 2), the matrix elements connecting them with other states (red arrows in Figure 10) are of the order of unity. The reason for such a strong rotation of main magnetic axes of the excited KD relative to the ground one, which strongly limits the SMM performance of **1** and **2** at elevated temperatures, is the presence of the Cy_3PO groups in the second coordination sphere (Figure 1). The full symmetrization of the second coordination sphere by replacement of these groups would result in a crystal field much closer to a D_{5h} symmetry, which will lead to parallel main magnetic axes in almost all KDs of the compound and, therefore, to a much higher blocking barrier.[31] Clearly, there is still enough room for significant improvement of the magnetization blocking performance of mononuclear lanthanide complexes.

■ CONCLUSION

Using these two complexes assembled from phosphine oxide, we have demonstrated how powerful the symmetry strategy can act by weakening the QTM and by enabling much more space

DOI: 10.1021/jacs.5b13584
J. Am. Chem. Soc. 2016, 138, 2829−2837

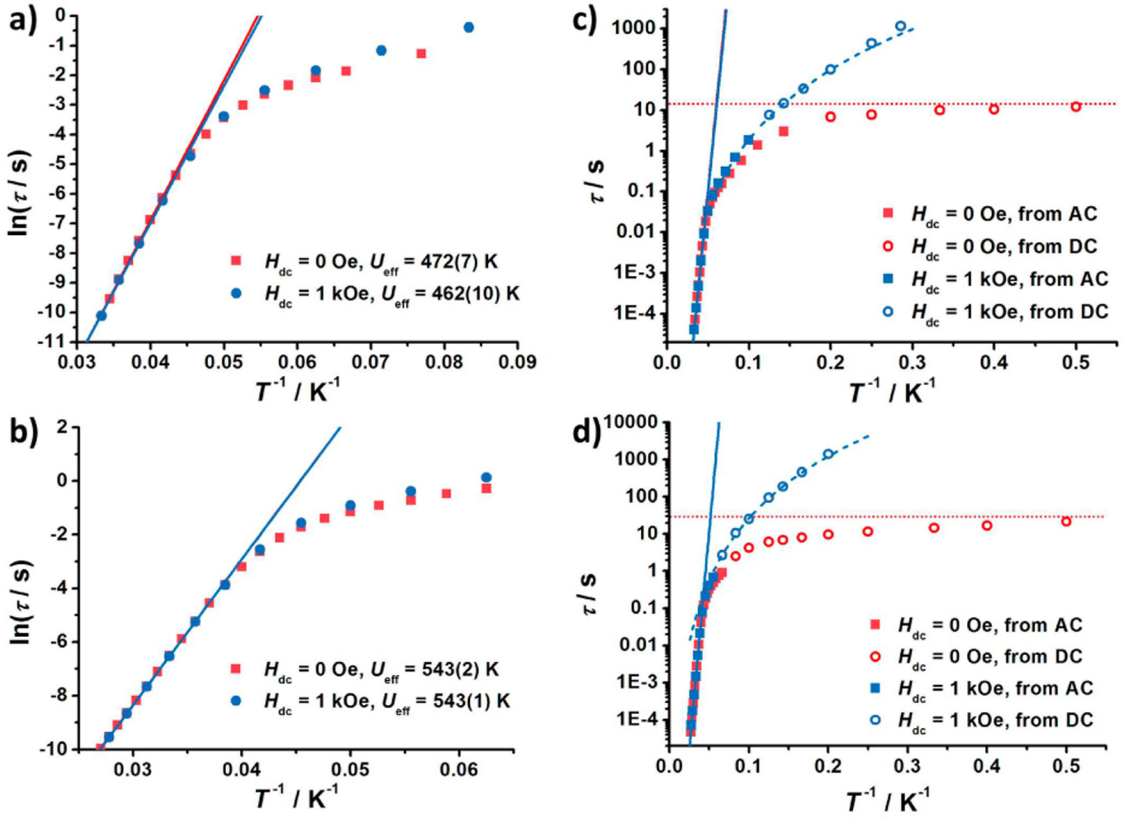

Figure 6. Temperature dependence of the relaxation time τ in a zero dc field (red) and a 1 kOe dc field (blue) for **1** (a,c) and **2** (b,d). The solid lines are the best fits to the Arrhenius law, the dashed lines are the best fits to the power law, and the dotted lines represent the limiting relaxation time set by QTM.

for the slow relaxation of magnetization in the design of SIMs. Although these two complexes only possess energy barriers of ~500 K, the observation of a magnetic hysteresis loop up to 20 K is undoubtedly the highlight among the other candidates. However, the lesson learned here is not a limit to such a specific system, and there are still countless strategies, such as replacing the R_3PO ligands, replacing the counterions, introducing negatively charged azial ligands,[27,34] and even using an isotope with zero nuclear spin, that can be adopted to further extend the limit; these strategies require continuous study. We can also foresee the possibility to cover the other lanthanide ions in such a family with (pseudo) 5-fold symmetry, setting up a giant database for deeper understanding of the magneto-structural correlations and the mechanism of slow magnetic relaxation. Furthermore, the design strategies of SIMs can also be applied to the wise assembly of multinuclear SMMs, where the inherent behavior of individual spin centers can be fine-tuned and further affected by intermetallic couplings to modify the behaviors of the whole molecule.[35] Finally, we note that the vast potential of classical coordination complexes in this field should not be ignored. They may seem simple, but with good design strategies, these complexes can also perform well as high performance molecular magnets, and their modifiability and stability are both highly valuable.

EXPERIMENTAL SECTION

General Procedure. All reagents were commercially available and used as received without further purification. The elemental analyses were performed with an Elementar Vario-EL CHN elemental analyzer. The IR spectra were recorded using a Thermo Nicolet AVATAR 330 FT-IR spectrometer. The powder XRD patterns were recorded on a Bruker D8 X-ray diffractometer with Cu Kα radiation. The ICP-AES analyses were performed with a TJA IRIS (HR) spectrometer. Thermogravimetric (TG) analysis was carried out on a NETZSCH TG209F3 thermogravimetric analyzer.

Synthesis. $[Dy(Cy_3PO)_2(H_2O)_5]Cl_3\cdot(Cy_3PO)\cdot H_2O\cdot EtOH$ (**1**) and $[Dy(Cy_3PO)_2(H_2O)_5]Br_3\cdot 2(Cy_3PO)\cdot 2H_2O\cdot 2EtOH$ (**2**) were synthesized based on the literature.[29] Hydrate DyX_3 (0.1 mmol, X = Cl for **1**, X = Br for **2**) and Cy_3PO (0.4 mmol) were dissolved in a H_2O/EtOH (1:9, 4 mL) mixed solution, followed by slow evaporation in ambient conditions. Colorless crystals suitable for X-ray analysis began to grow after 3 days and were then collected via filtration. The crystals were washed with cold EtOH and air-dried (yield ca. 30% for **1** and 40% for **2**). Further evaporation to less than 0.5 mL can significantly increase the yield, but the product is accompanied by a small amount of Cy_3PO. Analysis (calculated, experimental) for $H_{117}C_{56}O_{10}P_3Cl_3Dy$ (**1**): C (51.25, 50.87) and H (8.98, 8.98); for $H_{158}C_{76}O_{13}P_4Br_3Dy$ (**2**): C (50.53, 50.44) and H (8.82, 8.74). IR (cm^{-1}) for **1**: 3469br, 2927vs, 2852vs, 1643w, 1446s, 1107vs, 893m, 854m, 761m, 565m, 548m, 532m, and 445m; for **2**: 3226br, 2929vs, 2852vs, 1635w, 1448s, 1118s, 1099vs, 893m, 854m, 761m, 717m, 653m 565m, 548m, 534m, and 445m. The diluted samples **1**@Y and **2**@Y were synthesized in the same way, with the starting DyX_3:YX_3 = 1:19. The crystal structures were determined by the single-crystal diffraction as isostructral with **1** and **2**, respectively. The dilution ratios were confirmed by the magnetization and ICP-AES analyses as 5% ± 0.5%, and the phase purity was checked by the powder XRD.

X-ray Crystallography. Single-crystal diffraction data were recorded at 150(2) K on a Rigaku R-AXIS SPIDER Image Plate diffractometer with Mo Kα radiation, solved using direct methods, and refined using the SHELXTL program.[36] The contribution from the disordered solvent molecules in the voids was determined via elemental analysis and removed by the SQUEEZE routine using the PLATON program to proceed to the final refinement of the main structure.[37] Crystal data and structural refinement values are listed in

DOI: 10.1021/jacs.5b13584
J. Am. Chem. Soc. 2016, 138, 2829−2837

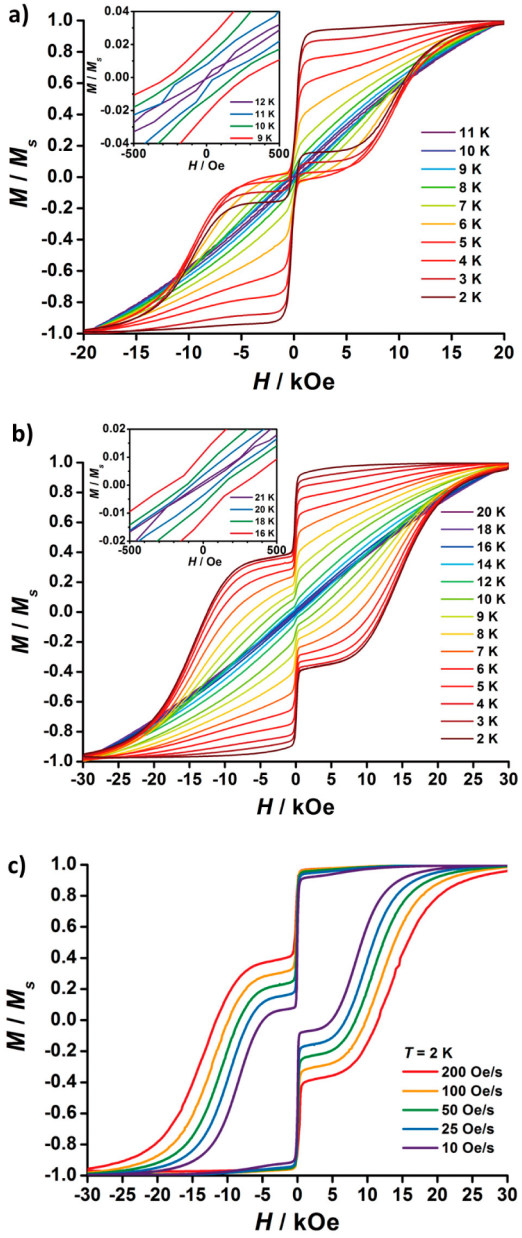

Figure 7. Normalized magnetic hysteresis loops for **1** (a) and **2** (b,c). The data were continuously collected at intervals of 1 s, with a field ramping speed of 200 Oe/s at various temperatures (a,b), and at 2 K for selected field ramping speeds (c). The expanded views (insets) reveal clear magnetic hysteresis to 11 K for **1** and 20 K for **2**. For all temperatures below, the loops are open at zero field.

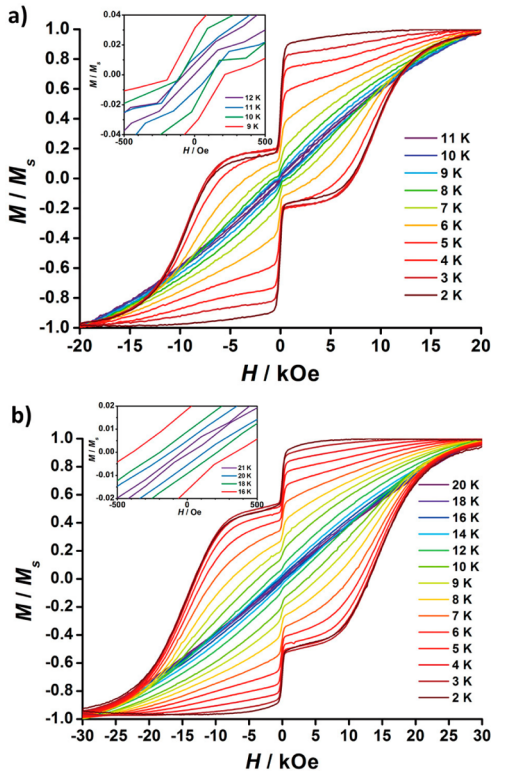

Figure 8. Normalized magnetic hysteresis loops for **1**@Y (a) and **2**@Y (b). The data were continuously collected at intervals of 1 s with the field ramping speed of 200 Oe/s at various temperatures. The expanded views (insets) reveal clear magnetic hysteresis to 11 K for **1**@Y and 20 K for **2**@Y. For all temperatures below, the loops are open at zero field.

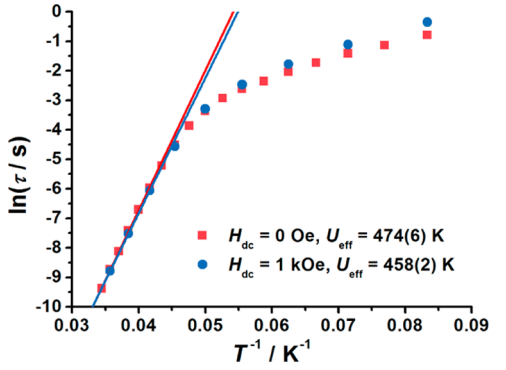

Figure 9. Temperature dependence of the relaxation time τ in a zero dc field (red) and a 1 kOe dc field (blue) for **1**@Y. The lines are the best fits to the Arrhenius law.

Tables S1 and S2. CCDC 1056944 (**1**), 1056945 (**2**), 1427206 (**1**@Y), and 1427207 (**2**@Y) contain the supplementary crystallographic data for this paper. These data can be obtained free of charge from the Cambridge Crystallographic Data Centre via www.ccdc.cam.ac.uk/data_request/cif.

Magnetic Measurements. The dc and ac magnetic measurements were performed on the polycrystalline samples using a Quantum Design MPMS XL-7 SQUID magnetometer. The ZFC-FC, hysteresis, and relaxation were measured using the Quantum Design PPMS with the VSM option. Diamagnetic correction was performed based on Pascal's coefficients.

***Ab Initio* Calculation.** Multiconfigurational wave function *ab initio* calculations were performed on the X-ray structures of **1** and **2** using the MOLCAS-8.0 quantum chemistry program package.[38] All calculations were of the CASSCF/RASSI/SINGLE_ANISO type. Contractions of the employed basis sets are provided in the SI. All atoms were described by the ANO-RCC relativistic basis sets[39] that are available in the MOLCAS package. Dy atoms and all neighboring ligand atoms were described with triple-ζ with polarization ANO-RCC basis sets while smaller double-ζ with polarization basis were employed for the distant ligand atoms. Large basis were also employed for the counterions (Br, Cl) and oxygen atom of the nonbonded ligands, to describe better the hydrogen bonding with the equatorial water molecules of **1** and **2**. The active space of the CASSCF method[37] included nine electrons from the last shell, spanning seven 4*f* orbitals of the Dy^{3+} ion. All spin states were optimized within state-averaged CASSCF calculations. Furthermore, all spin sextet, 128 spin quartet, and 130 spin doublet states were mixed via spin−orbit coupling in the RASSI program.[40] The resulting spin−orbital states were further used

DOI: 10.1021/jacs.5b13584
J. Am. Chem. Soc. 2016, 138, 2829−2837

Table 2. Energy and Magnetic Anisotropy of the Low-Lying Energy States Arising from the Ligand Field Splitting of the Ground Manifold J = 15/2 for 1 and 2, Obtained in the *Ab Initio* Calculations[a]

1			
energy (cm^{-1})	g_X	g_Y	g_Z
0	0.0008	0.0013	19.8632
267	0.4788	1.3270	15.9872
299	1.0420	1.4306	16.7249
368	3.0079	5.1975	11.0853
427	0.8597	3.5360	9.8732
455	0.2461	1.7602	13.0552
511	2.8034	4.0936	8.7893
533	2.0277	5.3359	11.8910
2			
energy (cm^{-1})	g_X	g_Y	g_Z
0	0.0003	0.0004	19.8762
250	0.3948	0.5865	18.9609
276	0.2220	0.3888	16.4704
378	1.7378	2.9928	14.7107
442	3.2470	4.9565	10.2983
467	2.8054	3.4509	11.6298
553	0.1555	1.4027	17.4021
580	0.5133	0.9406	18.0967

[a]Within the largest computational model. For results obtained in other computational models, see the SI.

Table 3. *Ab initio* Computed Crystal-Field Parameters for the Investigated Compounds[a]

		$B(k,q)$	
k	q	1	2
2	−2	0.3289	0.4143
2	−1	−0.5297	0.1628
2	0	**-0.1796×10^{1}**	**-0.1854×10^{1}**
2	1	0.2034	−0.4856
2	2	0.7529	0.2121×10^{1}
4	−4	-0.1276×10^{-2}	0.1230×10^{-2}
4	−3	**-0.1362×10^{-1}**	-0.6623×10^{-2}
4	−2	-0.1308×10^{-2}	-0.8645×10^{-3}
4	−1	0.2430×10^{-2}	-0.3469×10^{-3}
4	0	**-0.1148×10^{-1}**	**-0.1183×10^{-1}**
4	1	-0.1874×10^{-2}	0.6289×10^{-3}
4	2	-0.6060×10^{-3}	-0.2684×10^{-2}
4	3	**-0.1233×10^{-1}**	0.2568×10^{-2}
4	4	-0.5687×10^{-2}	-0.1463×10^{-2}
6	−6	-0.7524×10^{-4}	-0.1169×10^{-4}
6	−5	-0.6637×10^{-4}	-0.3162×10^{-4}
6	−4	-0.1670×10^{-4}	0.3569×10^{-5}
6	−3	-0.7668×10^{-4}	-0.4136×10^{-4}
6	−2	-0.1895×10^{-5}	-0.9690×10^{-5}
6	−1	0.1599×10^{-4}	-0.1845×10^{-4}
6	0	0.2174×10^{-4}	0.2298×10^{-4}
6	1	0.1433×10^{-4}	0.4717×10^{-4}
6	2	-0.2998×10^{-5}	-0.1261×10^{-4}
6	3	-0.7927×10^{-4}	0.2313×10^{-4}
6	4	-0.3287×10^{-4}	-0.1021×10^{-4}
6	5	-0.1625×10^{-3}	0.8597×10^{-5}
6	6	0.1057×10^{-3}	0.3085×10^{-4}

[a]Only the ranks k= 2, 4, and 6 are shown; higher ranks are much smaller and are not shown here.

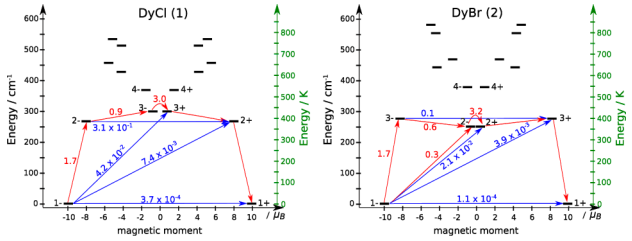

Figure 10. Magnetization blocking barriers for **1** (left) and **2** (right). Low-lying energy states arising from the ground atomic J = 15/2 have been arranged according to their magnetic moment (x axis) and energy (y axis). The arrows connecting the states represent various temperature-assisted relaxation processes possible for the investigated compounds. The numbers on the arrows represent the average value of the matrix element of the transition magnetic moment ($|\mu_x| + |\mu_y| + |\mu_z|$)/3. The most probable relaxation processes at high temperature follow the minimum energy path (red arrows), where the transition matrix elements connecting the states with opposite magnetization are the largest (see the discussion in the text).

by the SINGLE_ANISO[41] for computation of the local magnetic properties: **g**-tensor for ground and excited states, main magnetic axes, magnetic susceptibility, and molar magnetization; parameters of the crystal-field for the ground atomic multiplet.

■ ASSOCIATED CONTENT

Supporting Information

The Supporting Information is available free of charge on the ACS Publications website at DOI: 10.1021/jacs.5b13584.

Additional crystal structure data, magnetic characterization and ab initio calculations (PDF)
X-ray crystallographic data for **1** (CIF)
X-ray crystallographic data for **2** (CIF)
X-ray crystallographic data for **1**@Y (CIF)
X-ray crystallographic data for **2**@Y (CIF)

■ AUTHOR INFORMATION

Corresponding Authors

*ljliang1987@gmail.com
*Liviu.Ungur@chem.kuleuven.be
*tongml@mail.sysu.edu.cn

Notes

The authors declare no competing financial interest.

■ ACKNOWLEDGMENTS

This work was supported by the "973 Project" (2014CB845602 and 2012CB821704), the NSFC (Grant nos. 91122032, 21371183, and 91422302), the NSF of Guangdong (S2013020013002), and the Program for Changjiang Scholars and Innovative Research Team of the University of China. L.U. is a postdoc of the Fonds Wetenschappelijk Onderzoek-Vlaanderen and also gratefully acknowledges the INPAC and Methusalem grants of K.U. Leuven.

■ REFERENCES

(1) Gatteschi, D.; Sessoli, R.; Villain, J. *Molecular nanomagnets*; Oxford University Press: Oxford, 2006.
(2) Leuenberger, M. N.; Loss, D. *Nature* **2001**, *410*, 789.
(3) Wernsdorfer, W. *Science* **1999**, *284*, 133.
(4) Bogani, L.; Wernsdorfer, W. *Nat. Mater.* **2008**, *7*, 179.
(5) Mannini, M.; Pineider, F.; Sainctavit, P.; Danieli, C.; Otero, E.; Sciancalepore, C.; Talarico, A. M.; Arrio, M.-A.; Cornia, A.; Gatteschi, D.; Sessoli, R. *Nat. Mater.* **2009**, *8*, 194.

DOI: 10.1021/jacs.5b13584
J. Am. Chem. Soc. 2016, 138, 2829−2837

(6) Ganzhorn, M.; Klyatskaya, S.; Ruben, M.; Wernsdorfer, W. *Nat. Nanotechnol.* **2013**, *8*, 165.
(7) Sessoli, R.; Gatteschi, D.; Caneschi, A.; Novak, M. A. *Nature* **1993**, *365*, 141.
(8) Osa, S.; Kido, T.; Matsumoto, N.; Re, N.; Pochaba, A.; Mrozinski, J. *J. Am. Chem. Soc.* **2004**, *126*, 420.
(9) Ishikawa, N.; Sugita, M.; Ishikawa, T.; Koshihara, S.-y.; Kaizu, Y. *J. Am. Chem. Soc.* **2003**, *125*, 8694.
(10) Woodruff, D. N.; Winpenny, R. E. P.; Layfield, R. A. *Chem. Rev.* **2013**, *113*, 5110.
(11) Blagg, R. J.; Ungur, L.; Tuna, F.; Speak, J.; Comar, P.; Collison, D.; Wernsdorfer, W.; McInnes, E. J. L.; Chibotaru, L. F.; Winpenny, R. E. P. *Nat. Chem.* **2013**, *5*, 673.
(12) Jiang, S.-D.; Wang, B.-W.; Sun, H.-L.; Wang, Z.-M.; Gao, S. *J. Am. Chem. Soc.* **2011**, *133*, 4730.
(13) Layfield, R. A. *Organometallics* **2014**, *33*, 1084.
(14) Rinehart, J. D.; Fang, M.; Evans, W. J.; Long, J. R. *Nat. Chem.* **2011**, *3*, 538.
(15) Rinehart, J. D.; Fang, M.; Evans, W. J.; Long, J. R. *J. Am. Chem. Soc.* **2011**, *133*, 14236.
(16) Demir, S.; Zadrozny, J. M.; Nippe, M.; Long, J. R. *J. Am. Chem. Soc.* **2012**, *134*, 18546.
(17) Zadrozny, J. M.; Xiao, D. J.; Atanasov, M.; Long, G. J.; Grandjean, F.; Neese, F.; Long, J. R. *Nat. Chem.* **2013**, *5*, 577.
(18) Zadrozny, J. M.; Long, J. R. *J. Am. Chem. Soc.* **2011**, *133*, 20732.
(19) Poulten, R. C.; Page, M. J.; Algarra, A. G.; Le Roy, J. J.; López, I.; Carter, E.; Llobet, A.; Macgregor, S. A.; Mahon, M. F.; Murphy, D. M.; Murugesu, M.; Whittlesey, M. K. *J. Am. Chem. Soc.* **2013**, *135*, 13640.
(20) Westerström, R.; Dreiser, J.; Piamonteze, C.; Muntwiler, M.; Weyeneth, S.; Brune, H.; Rusponi, S.; Nolting, F.; Popov, A.; Yang, S.; Dunsch, L.; Greber, T. *J. Am. Chem. Soc.* **2012**, *134*, 9840.
(21) Jiang, S.-D.; Wang, B.-W.; Su, G.; Wang, Z.-M.; Gao, S. *Angew. Chem., Int. Ed.* **2010**, *49*, 7448.
(22) Chilton, N. F.; Langley, S. K.; Moubaraki, B.; Soncini, A.; Batten, S. R.; Murray, K. S. *Chem. Sci.* **2013**, *4*, 1719.
(23) Görller-Walrand, C.; Binnemans, K. In *Handbook on the Physics and Chemistry of Rare Earths*; Gschneidner, K. A., Eyring, L., Eds.; Elsevier: Amsterdam, 1996; Vol. *23*, p 121.
(24) AlDamen, M. A.; Clemente-Juan, J. M.; Coronado, E.; Martí-Gastaldo, C.; Gaita-Ariño, A. *J. Am. Chem. Soc.* **2008**, *130*, 8874.
(25) Meihaus, K. R.; Long, J. R. *J. Am. Chem. Soc.* **2013**, *135*, 17952.
(26) Ungur, L.; Le Roy, J. J.; Korobkov, I.; Murugesu, M.; Chibotaru, L. F. *Angew. Chem., Int. Ed.* **2014**, *53*, 4413.
(27) Liu, J.-L.; Chen, Y.-C.; Zheng, Y.-Z.; Lin, W.-Q.; Ungur, L.; Wernsdorfer, W.; Chibotaru, L. F.; Tong, M.-L. *Chem. Sci.* **2013**, *4*, 3310.
(28) Cardona-Serra, S.; Clemente-Juan, J. M.; Coronado, E.; Gaita-Ariño, A.; Camón, A.; Evangelisti, M.; Luis, F.; Martínez-Pérez, M. J.; Sesé, J. *J. Am. Chem. Soc.* **2012**, *134*, 14982.
(29) Lees, A. M. J.; Platt, A. W. G. *Polyhedron* **2014**, *67*, 368.
(30) Le Roy, J. J.; Ungur, L.; Korobkov, I.; Chibotaru, L. F.; Murugesu, M. *J. Am. Chem. Soc.* **2014**, *136*, 8003.
(31) Ungur, L.; Chibotaru, L. F. *Phys. Chem. Chem. Phys.* **2011**, *13*, 20086.
(32) Chilton, N. F. *Inorg. Chem.* **2015**, *54*, 2097.
(33) Ungur, L.; Thewissen, M.; Costes, J.-P.; Wernsdorfer, W.; Chibotaru, L. F. *Inorg. Chem.* **2013**, *52*, 6328.
(34) Gregson, M.; Chilton, N. F.; Ariciu, A.-M.; Tuna, F.; Crowe, I. F.; Lewis, W.; Blake, A. J.; Collison, D.; McInnes, E. J. L.; Winpenny, R. E. P.; Liddle, S. T. *Chem. Sci.* **2016**, *7*, 155.
(35) (a) Liu, J.-L.; Wu, J.-Y.; Chen, Y.-C.; Mereacre, V.; Powell, A. K.; Ungur, L.; Chibotaru, L. F.; Chen, X.-M.; Tong, M.-L. *Angew. Chem., Int. Ed.* **2014**, *53*, 12966. (b) Liu, J.-L.; Wu, J.-Y.; Huang, G.-Z.; Chen, Y.-C.; Jia, J.-H.; Ungur, L.; Chibotaru, L. F.; Chen, X.-M.; Tong, M.-L. *Sci. Rep.* **2015**, *5*, 16621.
(36) Sheldrick, G. *Acta Crystallogr., Sect. A: Found. Crystallogr.* **2008**, *64*, 112.
(37) Spek, A. *Acta Crystallogr.* **2015**, *C71*, 9.
(38) Aquilante, F.; De Vico, L.; Ferré, N.; Ghigo, G.; Malmqvist, P. å.; Neogrády, P.; Pedersen, T. B.; Pitoňák, M.; Reiher, M.; Roos, B. O. *J. Comput. Chem.* **2010**, *31*, 224. See also www.molcas.org.
(39) Roos, B. r. O.; Lindh, R.; Malmqvist, P.-Å.; Veryazov, V.; Widmark, P.-O.; Borin, A. C. *J. Phys. Chem. A* **2008**, *112*, 11431.
(40) Malmqvist, P. Å.; Roos, B. O.; Schimmelpfennig, B. *Chem. Phys. Lett.* **2002**, *357*, 230.
(41) Chibotaru, L. F.; Ungur, L. *J. Chem. Phys.* **2012**, *137*, 064112.

DOI: 10.1021/jacs.5b13584
J. Am. Chem. Soc. 2016, 138, 2829−2837